Appendix J

ANALYSIS OF INHIBITION OF FAULTING AT FAULT BRANCHES

Paul Somerville

ANALYSIS OF INHIBITION OF FAULTING AT FAULT BRANCHES

Paul Somerville, URS, 6 April 2009

Objective

The branching rupture scenario addressed in this study is one in which rupture begins on the main fault and branches onto the branch fault (with or without continuing to rupture on the main fault past the branch point). For Diablo Canyon, the scenario is one in which rupture begins on the Hosgri fault and branches onto the Shoreline fault. Other modes of branching, for example from the branch fault onto the main fault (e.g. Fliss et al., 2005), are not addressed in this study.

Method

We first compile a list of fault geometries with branch faulting and observed ruptures, including both cases in which there was rupture on the branch fault and cases in which there was no rupture on the branch fault. Next, we compare the observed cases with the predictions of the Kame et al. (2003) model to assess whether they are consistent with that model. For cases with rupture on the branch fault, we assess its impacts on ground motions recorded near the branch fault based on observed ground motions and previously published simulations.

The Kame et al (2003) Fault Branching Model

According to Kame et al (2003), branching of rupture from one fault to another can only occur under certain conditions. Poliakov *et al.* (2002) and Kame *et al.* (2003) have shown that the propensity of the rupture path to follow a fault branch is determined by the preexisting stress state, branch angle, and incoming rupture velocity at the branch location. The predictions of the Kame et al. (2003) model use the following three parameters:

Ψ = angle between the direction of maximum compressive stress (S_{max}) and the fault strike

φ = angle between the main fault and the branch fault

v_r = rupture velocity (expressed as a fraction of the shear wave velocity c_s)

The geometry of these parameters is shown in Figure 1.

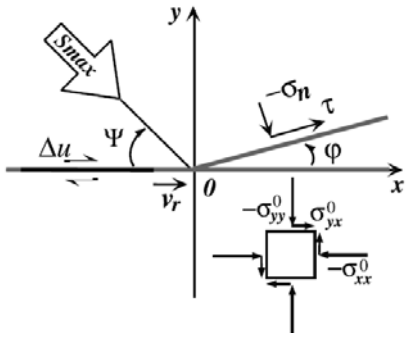

Figure 1. Configuration of a preexisting branched fault system and prestress state. Gray lines indicate potential rupture surface and black line indicates propagating rupture. Source: Kame et al. (2003).

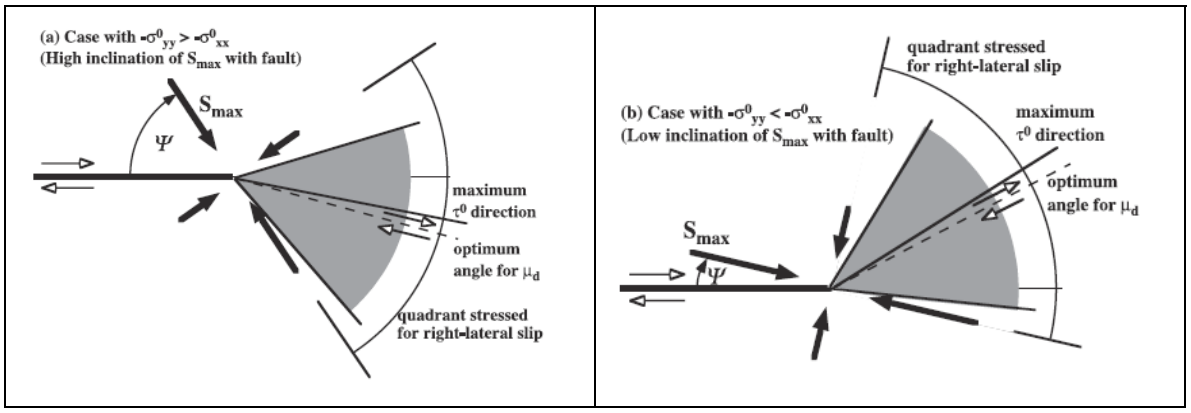

Figure 2. Qualitative prediction of the directions over which the larger scale prestress states favor right-lateral shear along bend paths. (a) Fault-normal precompression is dominant, $\Psi > 45^o$, allowing rupture to continue along bend paths primarily to the extensional side. (b) Fault-parallel precompression is dominant, $\Psi < 45^o$, allowing rupture to continue along bend paths primarily to the compressional side. The gray zones indicate the angle range where the initial shear stress is larger than the frictional resistance. Source: Kame et al. (2003).

As shown in Figure 2, values of $\Psi > 45^o$ generally favor branch faulting on the extensional side of the main fault, while values of $\Psi < 45^o$ generally favor branch faulting on the compressional side of the main fault. Figures 1 through 6 pertain to right-lateral faulting. For left-lateral faulting, these figures are rotated about the X axis.

The predictions of the model for four values of Ψ, namely 56^o, 45^o, 25^o and 13^o, are shown in Figures 3 through 6. In each case, the predictions are shown for each combination of four values of φ and three values of rupture velocity c_s. The values of φ are 30^o, 15^o, -15^o, and -30^o, and the values of v_r are $0.6c_s$, $0.8\ c_s$, and $0.9\ c_s$. The branch fault is on the compressional side of the fault for positive values of φ, and on the extensional side of the fault negative values of φ. These figures show final rupture traces in the vicinity of the intersection of the main fault with the branch fault. L_{stop} indicates the length of arrested rupture, given in terms of the slip-weakening zone size R_0 for low speed rupture along the main fault. Arrested rupture is indicated by the lines that have been highlighted in pink.

Application to the Kame et al. (2003) model to the Hosgri – Shoreline Fault Branch

Using the Kame et al (2003) model, branching of rupture from the Hosgri onto the Shoreline fault is physically prohibited under the current stress regime. Taking the S_{max} (orientation of the maximum compressional stress) to be N15E (McLaren, 2001), and strike angles of N25W for the Hosgri and N50W for the Shoreline fault, we obtain $\Psi = 45^o$ and $\varphi = +25^o$. These conditions pertain to Figure 4, top row, which shows rupture continuing on the main fault (shown in black) and strongly inhibited on the branch fault (shown in pink) for all three values of rupture velocity.

The statistics of fault branching angles in California have been analyzed by Ando et al. (2009). They find that fault branching angles have a skewed distribution of values that is approximately symmetrical on the compressional and dilatational sides of the fault, with a peak at 17^o.

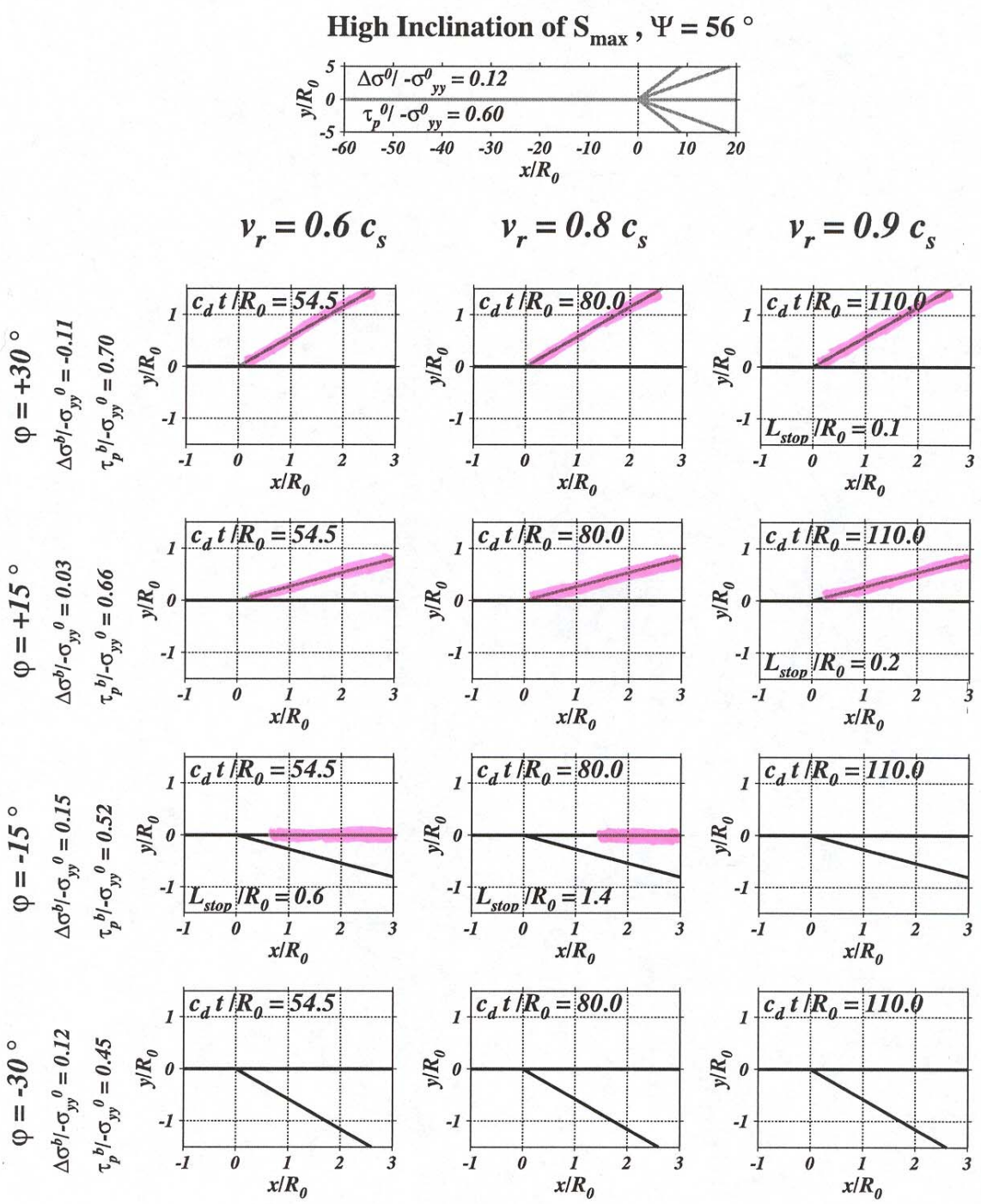

Figure 3. Diagram of final rupture traces in the vicinity of the intersection for cases with high inclination of Smax, $\Psi = 56^{o}$. L_{stop} indicates the length of arrested rupture once dynamically nucleated; those are given in terms of the slip-weakening zone size R_o for low-speed rupture along the main fault. Inhibition of fault rupture is shown by the pink highlighting. Source: Kame et al., 2003.

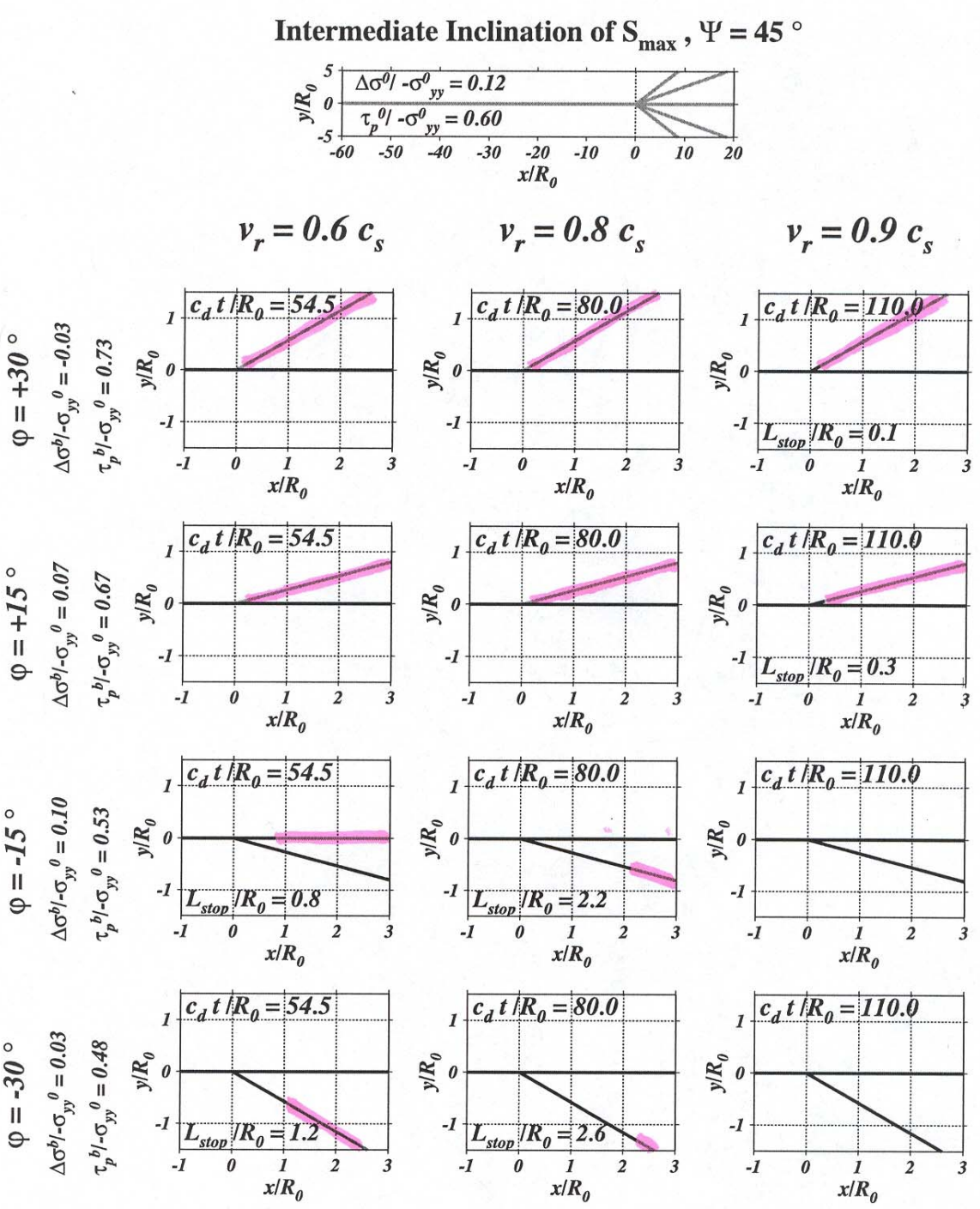

Figure 4. Diagram of final rupture traces in the vicinity of the intersection for cases with intermediate inclination of Smax, $\Psi = 45^{\circ}$. L_{stop} indicates the length of arrested rupture once dynamically nucleated; those are given in terms of the slip-weakening zone size R_o for low-speed rupture along the main fault. Inhibition of fault rupture is shown by the pink highlighting. Source: Kame et al., 2003.

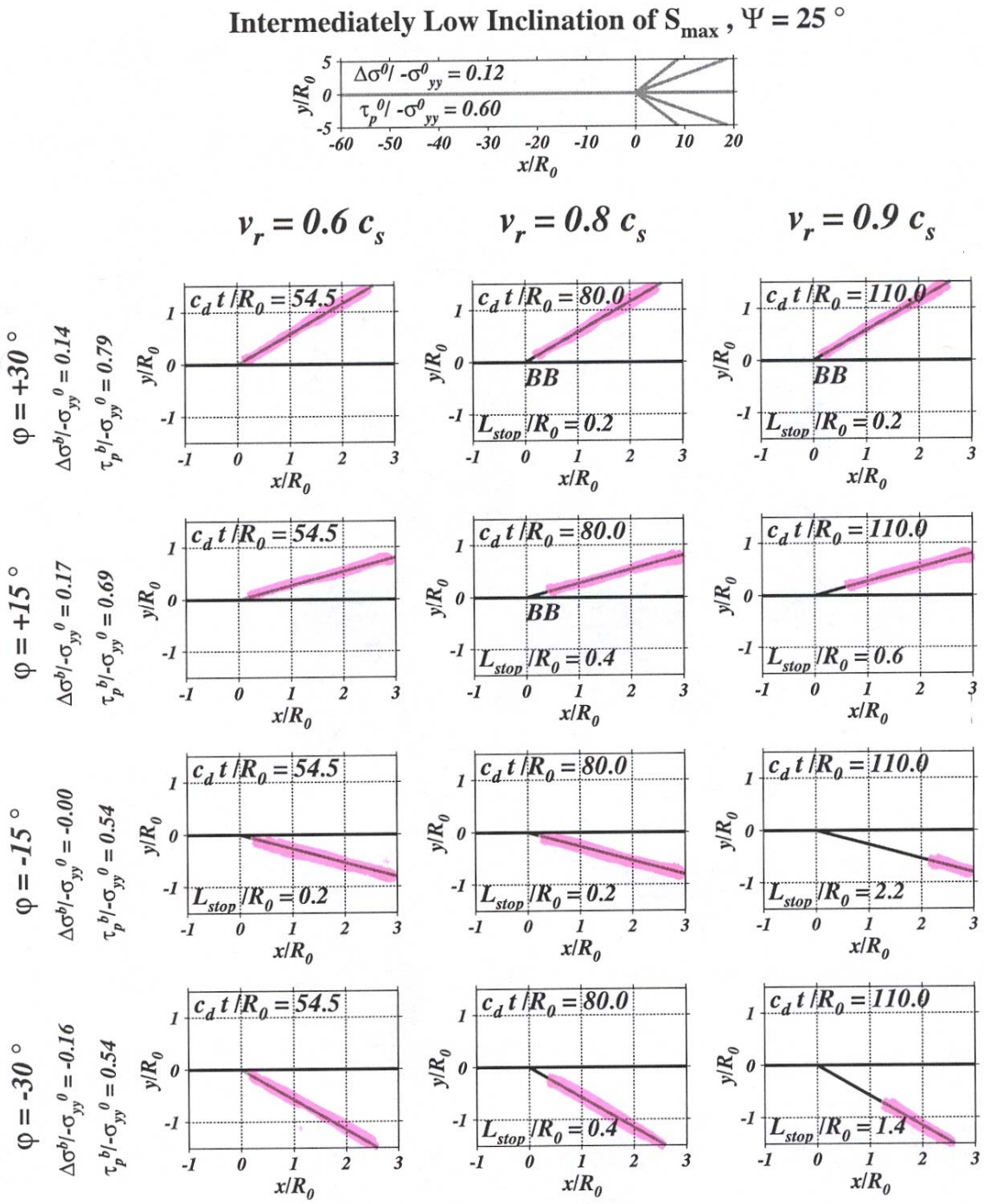

Figure 5. Diagram of final rupture traces in the vicinity of the intersection for cases with intermediately low inclination of Smax, Ψ = 25°. L_{stop} indicates the length of arrested rupture once dynamically nucleated; those are given in terms of the slip-weakening zone size R_o for low-speed rupture along the main fault. Inhibition of fault rupture is shown by the pink highlighting. Source: Kame et al., 2003.

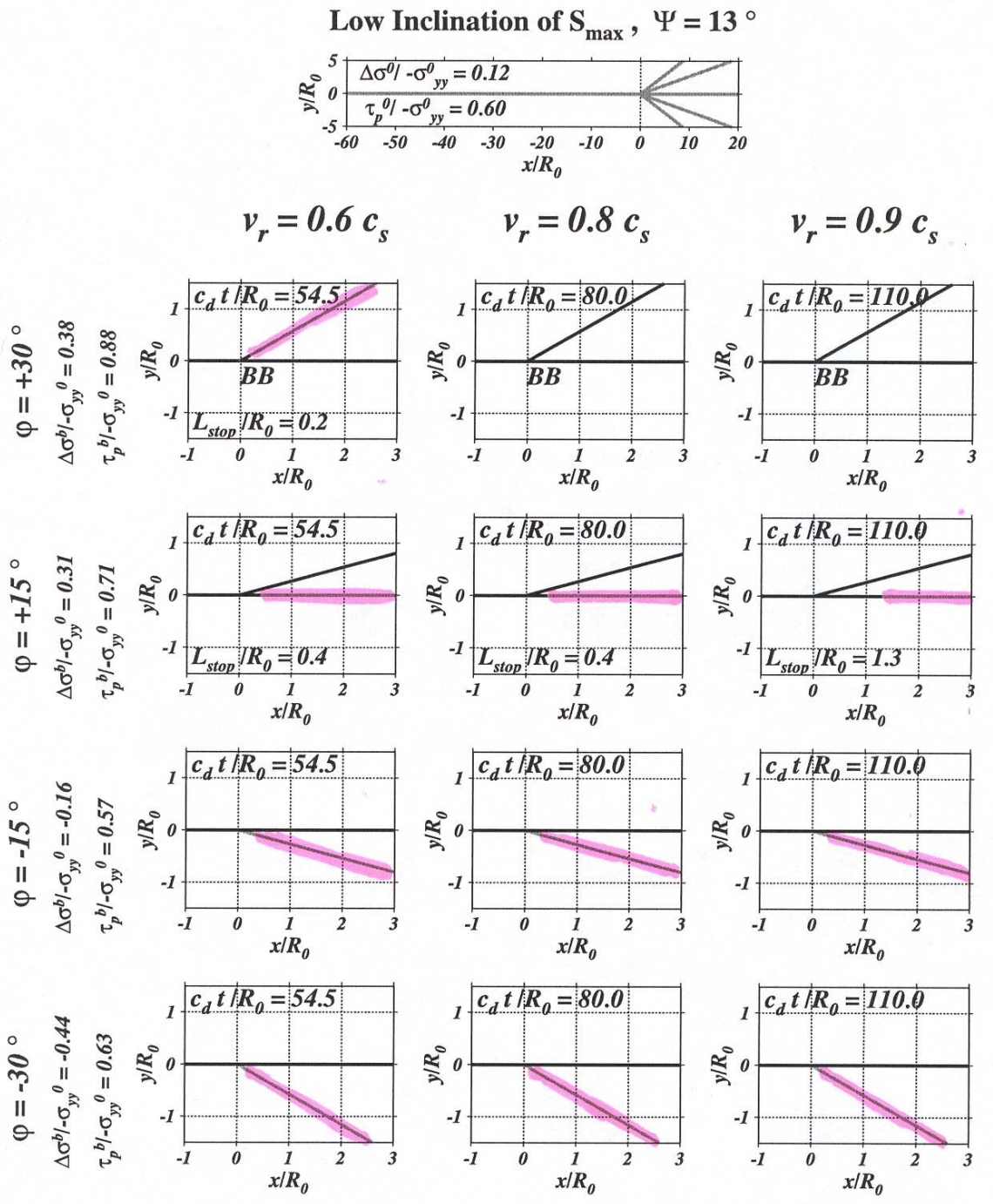

Figure 6. Diagram of final rupture traces in the vicinity of the intersection for cases with low inclination of Smax, $\Psi = 13^{o}$. L_{stop} indicates the length of arrested rupture once dynamically nucleated; those are given in terms of the slip-weakening zone size R_o for low-speed rupture along the main fault. Inhibition of fault rupture is shown by the pink highlighting. Source: Kame et al., 2003.

List of Fault Ruptures on Branched Faults

Wesnousky (2006; 2008) compiled information on the geometrical characteristics of a set of 37 earthquake surface rupture events, including 22 strike-slip events listed in Appendix 1. The main focus of these studies is on geometrical irregularities and their relationship to the termination of rupture. The focus of his studies was on stepovers, not on fault branching. The annotation of his fault maps states that adjacent and continuing traces of active faults that did not rupture during the earthquake are shown as dotted lines. However, this does not appear to consistently be the case, for example in the 1990 Luzon earthquake discussed further below. This limits the usefulness of his data compilation for the assessment of branch faulting in our study.

From the list of 22 strike-slip events in Appendix 1, we have selected six events involving rupture on branched faults, listed in Table 1. Bold fault names indicate that rupture proceeded on that fault past the branch point. All three possible modes of fault branching behavior are represented in these cases.

Mode 1. In three cases, including the 1979 Imperial Valley, 1995 Kobe, and 1992 Landers earthquakes, such rupture occurred on both the main fault and the branch fault (for the Kobe earthquake, the Gosukebashi segment represents the continuation of the Suwayama main fault segment).

Mode 2. In the 1990 Luzon and 2002 Denali earthquakes, rupture proceeded onto the branch fault but stopped on the main fault at the branch point.

Mode 3. In the 2001 Kokoxili (Kunlunshan) earthquake, the main fault continued to rupture without branching onto the Kitadan fault.

The mode 3 case is of most interest to Diablo Canyon, where we would like to know whether a southward rupture on the Hosgri fault would occur without branching onto the Shoreline fault.

Table 1. Earthquakes on branched faults

EVENT	MAIN FAULT	BRANCH FAULT	REFERENCE
1979 Imperial Valley	**Imperial**	**Brawley**	Kame et al., 2003
1990 Luzon	Philippine	**Digdig**	Rantucci, 1994
1995 Kobe	**Suwayama (Gosukebashi)**	**Okamoto**	Sekiguchi et al., 2000
1992 Landers	**Johnson**	**Kickapoo**	Kame et al., 2003
2001 Kokoxili (Kunlunshan)	**Kunlun**	Kitadan	Bhat et al., 2007
2002 Denali	Denali	**Totschunda**	Bhat et al., 2004

Comparison of Observations with Theoretical Models of Branch Faulting

1. 1979 Imperial Valley earthquake

Rupture in the 1979 Imperial Valley earthquake branched at the junction of the Imperial and Brawley faults, and surface and subsurface rupture proceed on both faults (Archuleta et al., 1984), as shown in Figure 7. The approximate S_{max} direction is poorly constrained but may be estimated to be approximately north-south, based on stress directions reported by Hardebeck and Hauksson (1999) along a profile somewhat to the northwest near the Salton Sea. That leads to $\Psi = 37^o$ with the main fault (the Imperial fault), where it branched, on the extensional side, at approximately $\varphi = -34^o$ onto the Brawley fault. This case corresponds to the results shown in Figure 4, last row, where the simulations show that progression of rupture on both the main fault as well as the branch is expected for all values of rupture velocity, and is enhanced by high values of rupture velocity. The model prediction is consistent with the observation that rupture continued on the main fault as well as branching onto the Brawley fault.

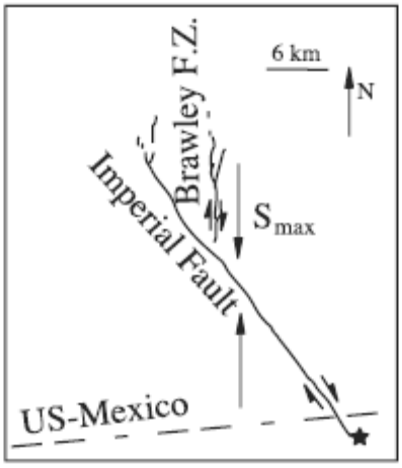

Figure 7. Fault geometry and maximum stress orientation, 1979 Imperial Valley earthquake. Source: Kame et al. (2003).

2. 1990 Luzon Earthquake

A location map of faults in Luzon is shown in Figure 8, and a rupture map of the 1990 Luzon earthquake is shown in Figure 9 (Rantucci, 1994). Rupture propagated northward on the Philippine fault and branched off that fault onto the Digdig fault near Rizal. The approximate S_{max} direction is poorly constrained in this region. Seno (1993) gives a value of about 300^o, consistent with the overall relative direction of about 294^o shown by Bird (2003), but measurements shown by Bird et al. (2003) on Luzon vary from 325^o in southeastern Luzon to 294^o in northwestern Luzon. Assuming a value of 294^o, and a strike of 310^o for the Philippine fault, we obtain $\Psi = 16^o$. The Digdig fault branches from the Philippine fault at an angle $\varphi = +15^o$ (the Philippine fault is a left-lateral fault, so the Dig-dig fault is on the compressional side). This case corresponds to the results shown in Figure 6, second row from the top, where the simulations show that progression of rupture only on the branch is expected for values of rupture velocity of $0.6c_s$ and $0.8c_s$. For these conditions, the model prediction is consistent with the observation that rupture branched onto the Digdig fault without continuing on the Philippine fault. For a rupture

velocity of $0.9c_s$, there is weak tendency for rupture to also propagate on the main fault. If the direction of is Ψ as much as 25^o, which is within its range of uncertainty, then the Kame et al. (2003) model would predict rupture to continue on the Philippine fault without branching onto the Digdig fault.

The locations of previous earthquakes on the Philippine fault are shown in Figure 9. The segment of the Philippine fault south of Rizal broken by the 1990 earthquake previously broke in 1645, whereas segments of the Philippine fault north of Rizal, which did not break in 1990, previously ruptured more recently, in 1796 and 1892 earthquakes. This suggests that branching off the Philippine fault onto the Digdig fault in the 1990 earthquake may also have been influenced by the preexisting stress state on the Philippine fault.

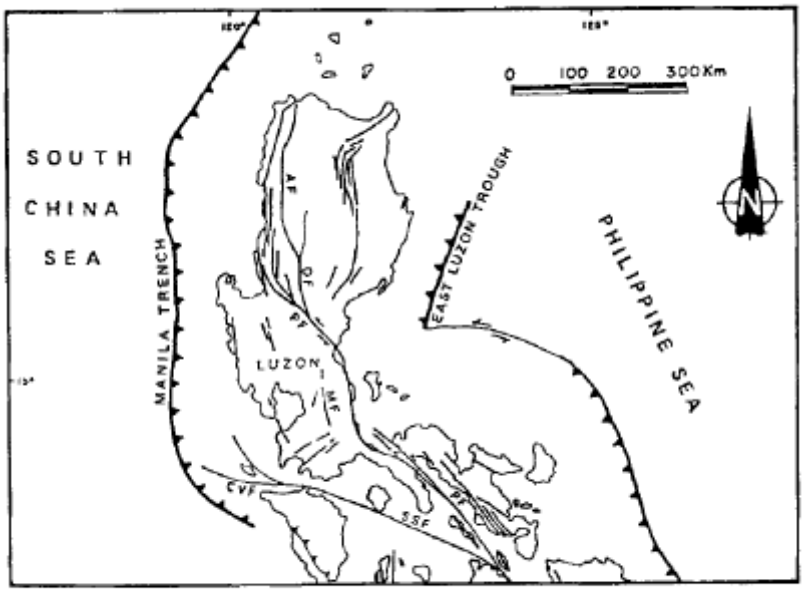

Fig.4.8 - *Major tectonic lineaments in Luzon (PF = Philippine Fault, DF = Digdig Fault, AF = Abra Fault, MF = Manila Fault), from Punongbayan and Umbal (1990).*

Figure 8. Location map of the 1990 Luzon earthquake. Rupture propagated northward on the Philippine fault (PF) and branched onto the Digdig fault (DF). Source: Rantucci (1994).

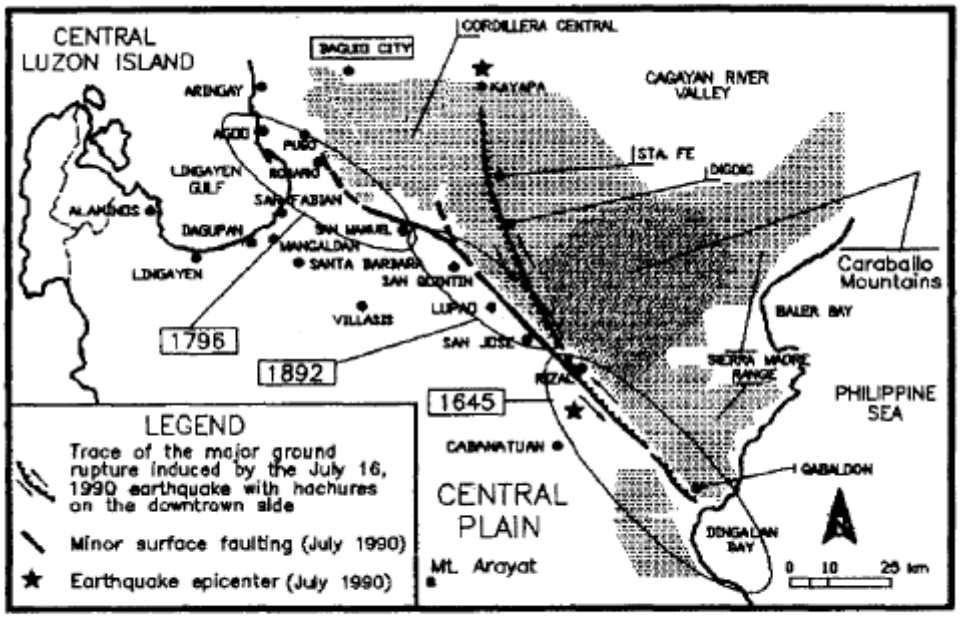

Fig. 4.9 – *Location of the Major Ground Rupture and minor surface faultings in Central Luzon associated with the July 1990 earthquake and the areas affected by the 1645, 1796, 1892 earthquakes.*

Figure 9. Rupture map of the 1990 Luzon earthquake. Rupture propagated northward on the Philippine fault and branched off that fault onto the Digdig fault near Rizal. The locations of the 1645, 1796 and 1892 earthquakes are also shown. Source: Rantucci (1994).

3. 1995 Kobe earthquake

A fault model of the 1995 Kobe earthquake was developed by Sekuguchi et al. (2000), shown in Figures 10 and 11. The fault model is divided into four main segments, A, B, C, and D (respectively corresponding to the Nojima, Suma, Suwayama, and Gosukebashi faults), and a branch segment, E, corresponding to the Okamoto fault. Of these five fault segments, only the Nojima fault (on Nojima Island) had surface faulting. Rupture of the remaining segments is inferred from aftershock locations, geodetic data, and the constraints on the location of the intersection of the causative fault planes and the earth surface in the Kobe City area obtained by Sekiguchi *et al.* (1996a, b). Sekiguchi et al. (2000) showed that inclusion of rupture on the branching Okamoto fault provided an improved fit to seismological and geodetic data.

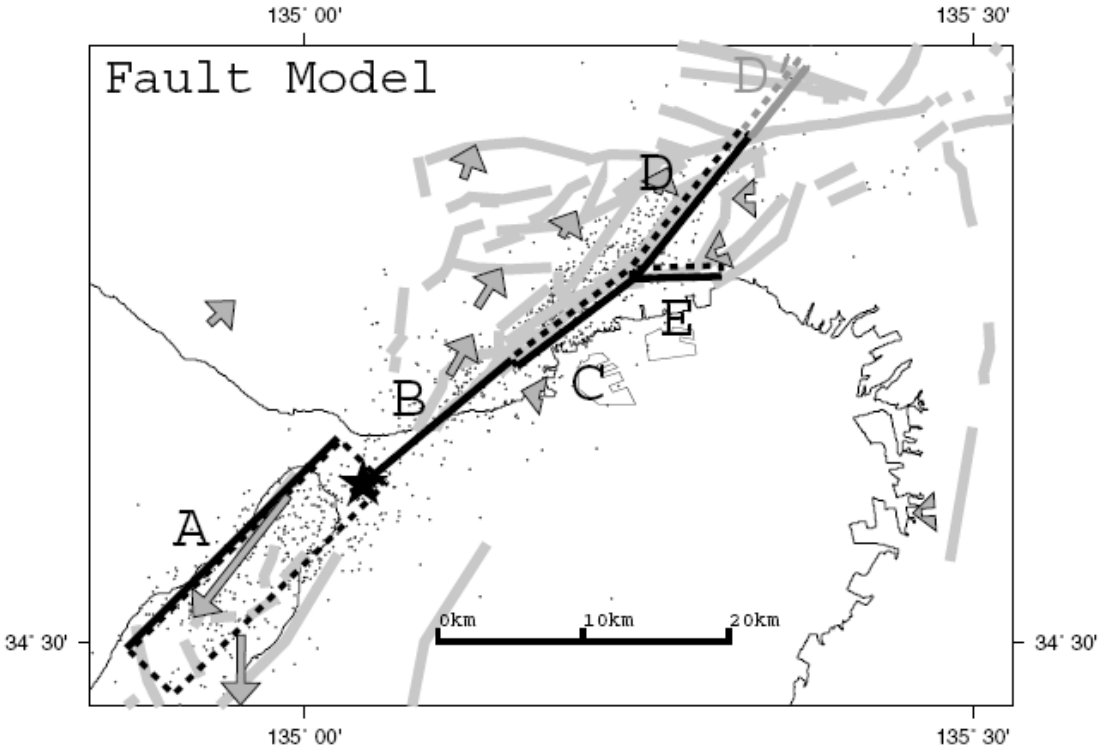

Figure 10. Fault-plane model (with segments A, B, C, D, and E). Black and gray lines show the active-fault traces reported by Ishihara *et al.* (1991). The black lines are those estimated to be causative faults. Vectors show static displacements during 1984 and 1995 after the earthquake, as determined by Hashimoto et al. (1996) from GPS data. Epicenters of the mainshock and aftershocks during the day of the mainshock are those determined by Nemoto et al. (1996, 1997). Dots are epicenters of aftershocks that occurred within 18 hours after the mainshock. Source: Sekiguchi et al., 2000.

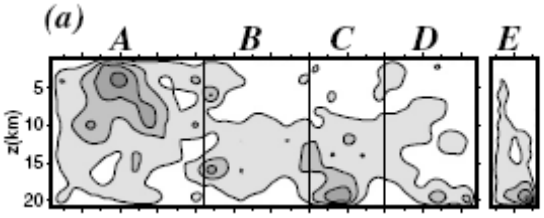

Figure 11. Final moment release distribution for the fault model with segments A, B, C, D, and E. Source: Sekiguchi et al., 2000.

The fault geometry of the branching fault is shown in Figure 10 (Sekiguchi et al., 1984). The approximate S_{max} direction is east-west, based on stress directions reported by Seno (2002). That leads to $\Psi = 37^{o}$ with the main fault (taken as the Suwayama segment), where it branched on the extensional side onto the Okamoto fault. Measured with respect to the strike of the Suwayama fault, the branching angle φ is -35^{o}, but measured with respect to the Gosukebashi fault, the branching angle $\varphi = -50^{o}$. The change in strike of the main fault (between the Suwayama and Gosukebashi faults) at the fault branch is 35^{o}. The model of Kame et al. (2003) assumes that the main fault is straight, so their calculations may not be completely applicable to the Kobe earthquake. This case

corresponds approximately to Figure 4, last row, where the simulations show that progression of rupture on both the main fault as well as the branch is expected for all values of rupture velocity, and is enhanced by high values of rupture velocity. The model prediction is consistent with the inference by Sekiguchi et al. (2000) that rupture branched onto the Okamoto fault as well as continuing on the Gosukebashi fault.

4. 1992 Landers earthquake

The fault geometry of the Landers earthquake, based on Sowers et al. (1994), is shown in Figure 12. S_{max} is taken from stress orientations in the Landers region determined by Hardebeck and Hauksson (2001) to be at approximately $\Psi = 60^{o}$ with the trace of the Johnson Valley fault where it branched to the extensional side onto the Kickapoo fault, with the angle $\varphi = -30^{o}$. The rupture also continued a few kilometers on the main (Johnson Valley) fault. This case corresponds to the results shown in Figure 3, last row, where the simulations show that progression of rupture on both the main fault as well as the branch is expected for all values of rupture velocity. The model prediction is consistent with the observation that rupture continued on the main fault as well as branching onto the Kickapoo fault.

Rupture died out on the Johnson Valley Fault a short distance after branching, which remains unexplained by the model. However, Kame et al. (2003) cited King et al.'s (1994) finding that a region of negative stress change occurs on the northwest continuation of the Johnson Valley Fault. The dynamic rupture was arrested shortly after propagating into that region of negative stress change. The negative stress changes are modest, of the order of 0.1 MPa, but may be related to why the rupture arrested.

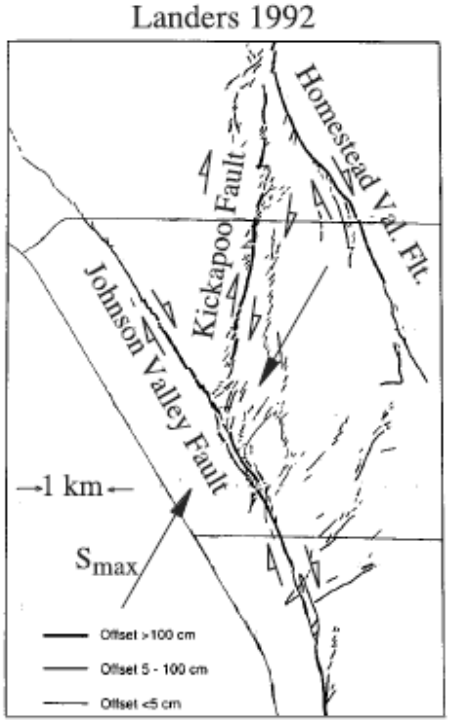

Figure 12. Fault geometry and maximum stress orientation, 1992 Landers earthquake. Source: Kame et al. (2003).

5. 2001 Kokoxili (Kunlunshan) Earthquake

Rupture propagated eastward on the Kunlun fault past its junction with the Kitadan fault, without branching onto the Kitadan fault (Xu et al., 2002; Bhat et al., 2007; Figure 13). The stepover of a few km between the Kunlun and Kitadan fault is considered to be insufficient to have hindered branching. The maximum compression direction Ψ with respect to the strike of the Kunlun fault near the junction was estimated by Bhat et al. (2007) to range from approximately 30^o to 45^o. The branching angle of the Kitadan fault is $\varphi = -10^o$. This case corresponds to Figure 4 or 5, third row from top. In Figure 5, for $\Psi = 25^o$, rupture on the branch fault is inhibited for $Vr = 0.6c_s$ and $0.8c_s$, and partly inhibited for $Vr = 0.9c_s$. In Figure 4, for $\Psi = 45^o$, rupture on the branch is inhibited only for partly and only for $Vr = 0.8c_s$. The model prediction may be consistent with the observation that rupture continued on the main fault without branching onto the Kitadan fault. It is also possible that the rupture velocity was supershear at the fault branching point (Bouchon and Vallee, 2003). More information about this case is needed to obtain a definitive conclusion.

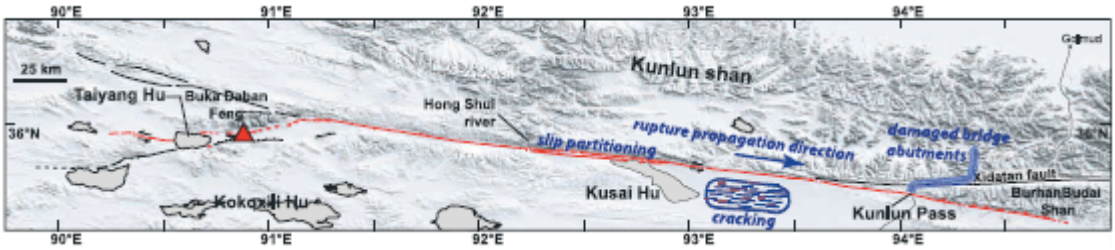

Figure 13. Simplified map of the surface rupture (red line) for the 2002 Kokoxili earthquake (adapted from Klinger et al. [2005]). Epicenter is indicated by a red triangle so that rupture propagated mainly to the east

6. 2002 Denali earthquake

Bhat et al. (2004) analyzed the observed dynamic slip transfer from the Denali to Totschunda faults during the *M*w 7.9 3 November 2002 Denali fault earthquake, Alaska (Figure 14). They used 2D numerical simulations of the rupture processes in the vicinity of the branch junction. The angle Ψ between the maximum compression direction and the strike of the Denali fault near the junction was estimated to be 70^o and 80^o for their numerical simulations. The rupture velocity at branching is not well constrained but has been estimated to average about $0.8c_s$ throughout the event. They used values of $0.6c_s$ $0.8c_s$, $0.9c_s$ and $1.4\ c_s$ in their simulations. The assumed branching angle of the Totschunda fault was $\varphi = 15^o$. Except for 70^o and $0.9c_s$, all of their simulations predicted that the rupture path branches off the Denali fault onto the Totschunda fault. For all of these conditions, the model prediction is consistent with the observation that rupture branched onto the Totschunda fault without continuing on the Denali fault. For 70^o and $0.9c_s$, rupture continued on the Denali fault as well as branching onto the Totschunda fault, but the rupture speed on the Denali fault was slower than that along the Totschunda fault and the slip was less.

The calculations of Kame et al. (2003) do not cover angles Ψ as large as 70^o and 80^o. The Denali case corresponds most closely to the results for $\Psi = 54^o$ shown in Figure 3,

third row from the top, where the simulations show that progression of rupture mainly on the branch is expected for values of rupture velocity of $0.6c_s$ and $0.8c_s$, with a weak tendency for rupture to propagate on the main fault. For these conditions, the model prediction is consistent with the observation that rupture branched onto the Totschunda fault without continuing on the Denali fault. For a rupture velocity of $0.9c_s$, there is weak tendency for rupture to also propagate on the main fault.

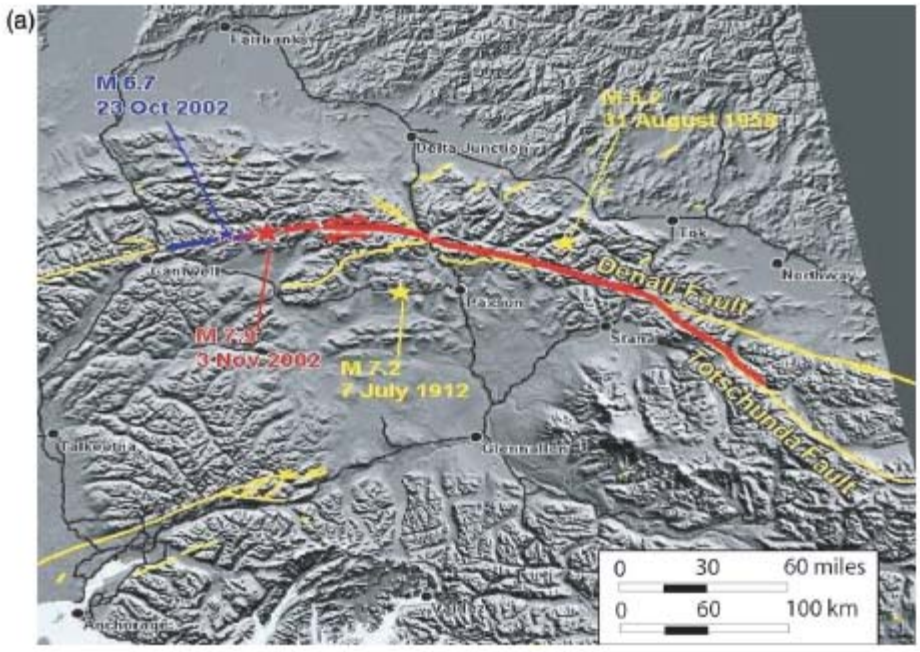

Figure 14. Rupture path, shown as a solid red line, of the *M*w 7.9 Denali fault earthquake. The star near the western end of the rupture marks the epicenter. Source: Bhat et al. (2004).

Impacts of Fault Branching on Ground Motions

1. 1979 Imperial Valley Earthquake, Brawley Fault

Although the Brawley fault contributes only about 4% of the total seismic moment, it has a marked effect on the ground motion of nearby stations. Figure 15 shows the calculated contributions from the Brawley fault at stations of the El Centro array. At station E05, the 53° component was most affected, whereas the 323° component at E06 was most affected. This was explained as resulting from radiation pattern effects by Archuleta (1984). Figure 16 illustrates the contribution of the Brawley fault to the total motion at stations E06 and E07. The total synthetic seismogram is divided into the contributions from the Imperial fault and from the Brawley fault. The Brawley fault made a large contribution to the peak velocity on the 323° component at E06, and to the 53° component at E05 (not shown in Figure 16, but indicated in Figure 15).

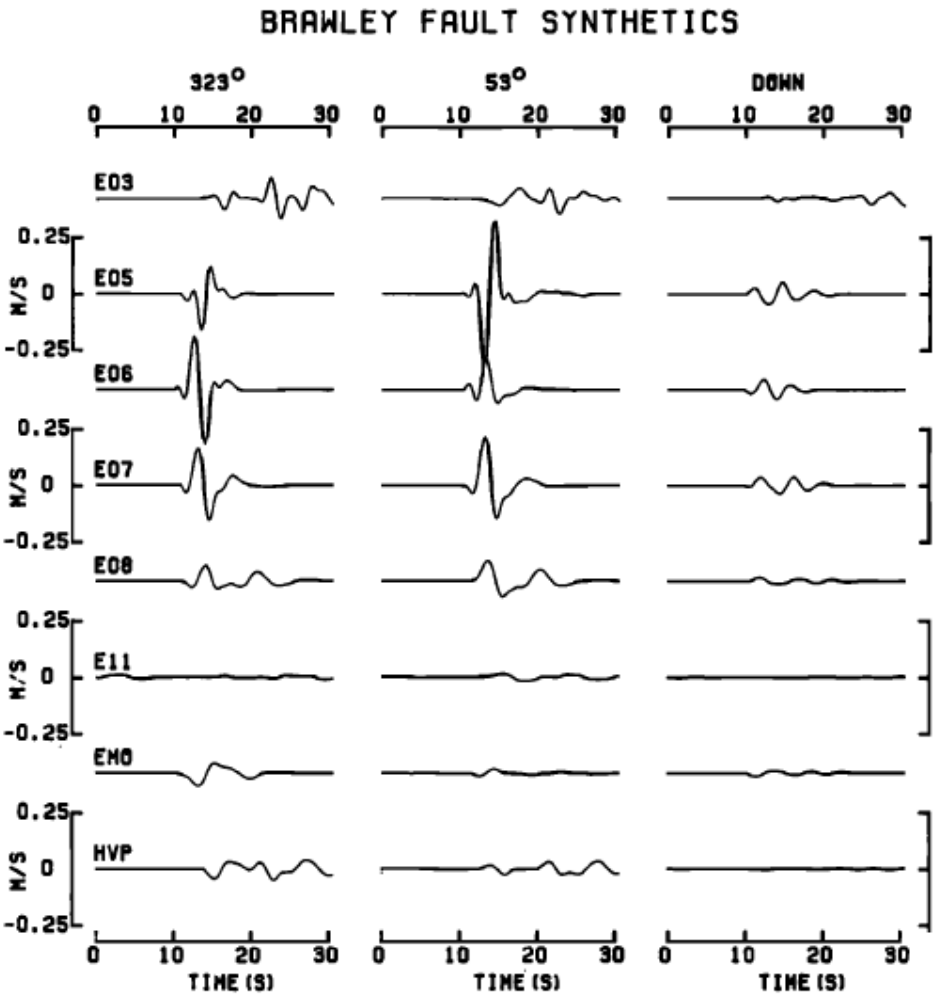

Figure 15. Calculated contributions of the Brawley fault to the ground velocity recorded at strong motion recording stations of the El Centro array. Source: Archuleta (1984).

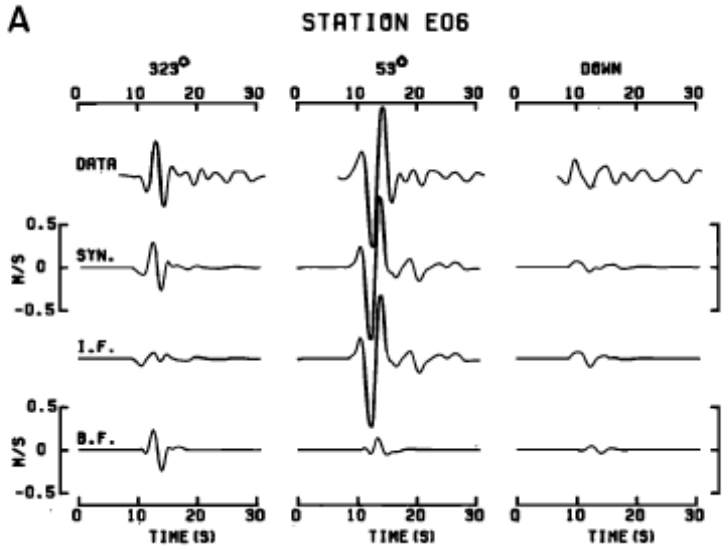

Figure 16. Calculated contributions of the Brawley and Imperial faults to the ground velocity recorded at station E06. Source: Archuleta (1984).

2. Kobe Earthquake – Okamoto fault

Sekiguchi et al. (2000) simulated the near-source ground motion using 3-D FDM (Pitarka *et al.,* 1998) to estimate the effect of slip on the Okamoto fault on the ground motions, based on Iwata et al. (1999). The slip on the Okamoto fault affected the ground motion in the eastern part of Kobe (Nada and Higashi-Nada wards), Ashiya, and Nishinomiya cities, but its contribution was not dominant, even in those regions, constituting about 30 to 50% of the maximum velocity at 0.1 to 1.0 Hz. Figure 17 shows the contribution of the Okamoto fault (segment E) to the total synthetic ground velocities at station KBU. The contribution is about 30% on the North component, and very small on the east component. The contributions of each fault segment to the calculated peak velocity throughout the region is shown in Figure 18.

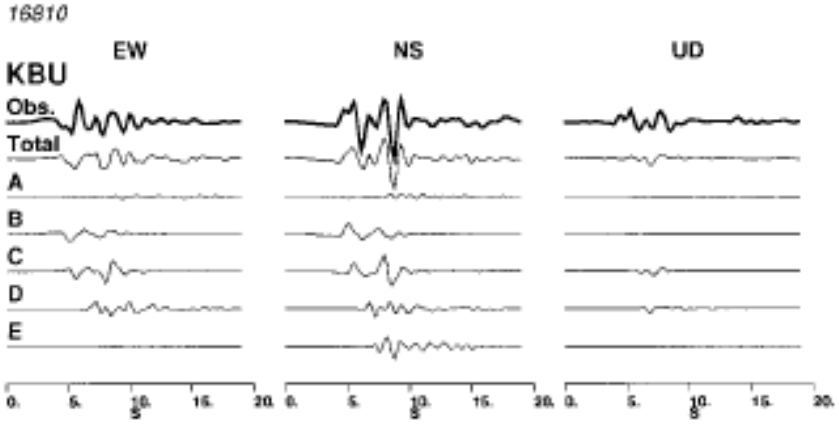

Figure 17. Observed (bold line) and synthetic (thin line) waveforms at KBU station. From the top: observed, synthetics for all 5 segments (ABCDE), and synthetics from segments A, B, C, D, and E (Okamoto segment). Source: Sekiguchi et al. (2000).

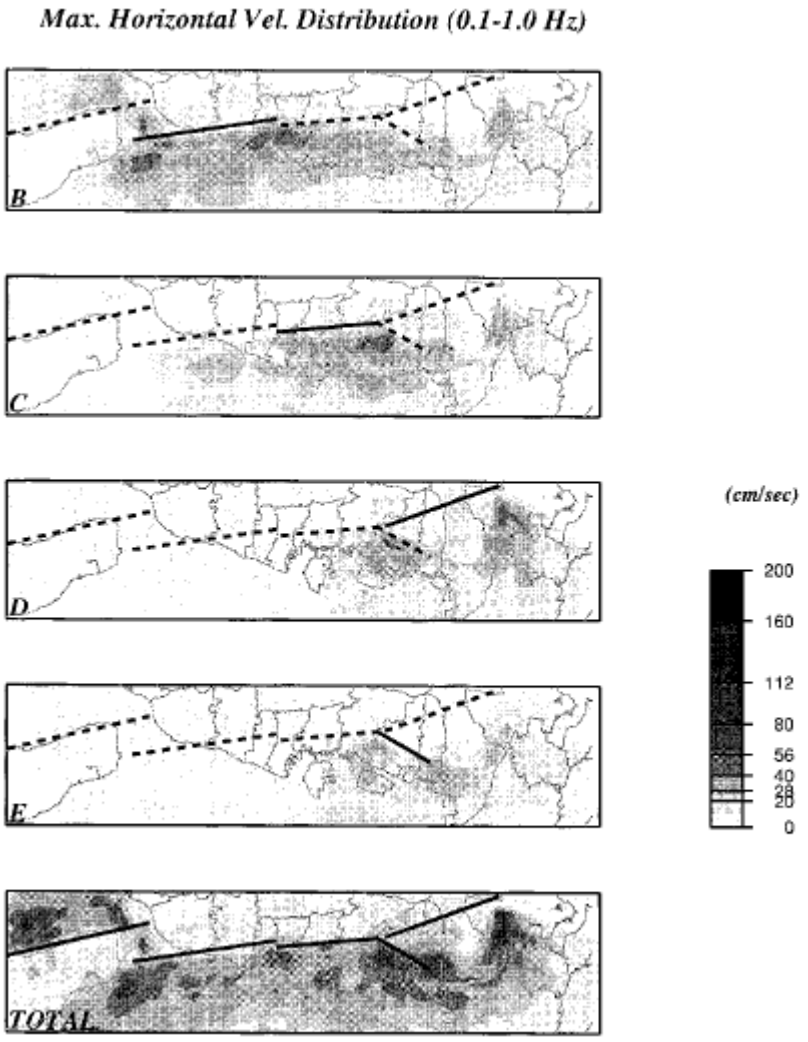

Figure 18. Distribution of the maximum horizontal velocity from each segment of the source. From top to bottom: distributions of maximum horizontal velocity caused by slip on Segments B, C, D, and E (Okamoto segment) and on the entire source. Source: Sekiguchi et al. (2000).

Conclusions

We have analyzed six events involving rupture on branched faults which represent three possible modes of fault branching behavior. In three cases, including the 1979 Imperial Valley, 1995 Kobe, and 1992 Landers earthquakes, such rupture occurred on both the main fault and the branch fault. In all three of these cases, the observations are consistent with the Kame et al. (2003) model. In the 1990 Luzon and 2002 Denali earthquakes, rupture proceeded onto the branch fault but stopped on the main fault at the branch point. The Denali earthquake observations are consistent with the Kame et al. (2003) model, and the Luzon earthquake observations are also potentially consistent, but the uncertainty in the stress field orientation renders this inconclusive with current data.

In the 2001 Kokoxili (Kunlunshan) earthquake, the main fault continued to rupture without branching onto the Kitadan fault. The Kokoxili earthquake observations are potentially consistent with the Kame et al. (2003) model, but the uncertainty in the stress field orientation renders this inconclusive with current data. The Kokoxili earthquake is the only case of the six that is directly relevant to the Hosgri – Shoreline branch, where we expect that rupture will continue on the main fault and be inhibited on the branch fault.

In the cases of the Imperial Valley and Kobe earthquakes, the contribution of the branch fault to the ground motions of the earthquake as a whole appear to have been locally fairly large, up to about one-half the overall ground motion level.

References

Ando, R., B.E. Shaw and C.H. Scholz (2009). Quantifying natural fault geometry: statistics of splay fault angles. *Bull. Seism. Soc. Am.*, 99, 389-395.

Archuleta, R.J. (1984). A faulting model for the 1979 Imperial Valley earthquake, *J. Geoph. Res.*, 89, 4559-4585.

Bhat, H.S., R. Dmowska, G.C.P. King, Y. Klinger, and J.R. Rice (2007). Off-fault damage patterns due to supershear ruptures with application to the 2001 M_w 8.1 Kokoxili (Kunlun) Tibet earthquake, *J. Geoph. Res.*, 112, B06301, doi:10.1029/2006JB004425.

Bhat, H.S., R. Dmowska, J.R. Rice, and N. Kame (2004). Dynamic slip transfer from the Denali to Totschunda Faults, Alaska: testing theory for fault branching, *Bull. Seism. Soc. Am.*, 94(6B), S202-S213.

Bhat, H.S., M. Olives, R. Dmowska, and J.R. Rice (2007). Role of fault branches in earthquake rupture dynamics, *J. Geoph. Res.*, 112, B11309, doi:10.1029/2007JB005027.

Bird, P. (2003) An updated digital model of plate boundaries, *Geochemistry Geophysics Geosystems*, *4*(3), 1027, doi:10.1029/2001GC000252.

Bouchon, M. and M. Vallee (2003). Observation of long supershear rupture during the magnitude 8.1 Kunlunshan earthquake. Science 301, 824-826.

Fliss, S., H.S. Bhat, R. Dmowska, and J.R. Rice (2005). Fault branching and rupture directivity, *J. Geoph. Res.*, 110, B06312, doi:10.1029/2004JB003368.

Hardebeck, J. L., and E. Hauksson, Crustal stress field in southern California and its implications for fault mechanics, J. Geophys. Res., 106, 21,859–21,882, 2001.

Hardebeck, J. L., and E. Hauksson, Role of fluids in faulting inferred from stress field signatures, Science, 285, 236– 239, 1999.

Iwata, T., H. Sekiguchi, A. Pitarka, and K. Irikura (1999). Ground motion simulations in the Kobe area during the 1995 Hyogoken-Nanbu earthquake, in *The Effects of Surface Geology on Seismic Motion,* Irikura K., K. Kudo, H. Okada, and T. Sasatani (Editors), Vol. 3, BALKEMA, Rotterdam, 1295–1310.

Kame, N., J.R. Rice and R. Dmowska (2003). Effects of prestress state and rupture velocity on dynamic fault branching. J. Geophys. Res. 108, ESE 13-1 – 13-21.

McLaren, M.K. and W.U. Savage (2001). Seismicity of south-central coastal California: October 1987 through January 1997. *Bull. Seism. Soc. Am.*, 91(6), 1629-1658

Pitarka, A., K. Irikura, T. Iwata, and H. Sekiguchi (1998). Three-dimensional simulation of the near-fault ground motion for the 1995 Hyogoken Nanbu (Kobe), Japan, earthquake, *Bull. Seism. Soc. Am.* **88,** 428– 440.

Poliakov, A. N. B., R. Dmowska, and J. R. Rice, Dynamic shear rupture interactions with fault bends and off-axis secondary faulting, J. Geophys.Res., 107(B11), 2295, oi:10.1029/2001JB000572, 2002.

Rantucci, Giovanni (1994). Geological disasters in the Philippines : The July 1990 earthquake and the June 1991 eruption of Mount Pinatubo. Rome, Italy.

Sekiguchi, H., K. Irikura, and T. Iwata (2000). Fault geometry at the rupture termination of the 1995 Hyogo-ken Nanbu earthquake, *Bull. Seism. Soc. Am.*, 90(1), 117-133.

Seno, T. (2002). Synthesis of the regional stress fields of the Japanese islands. *Island Arc*, 8, 66-79.

Seno, T., S. Stein and A. Gripp (1993). A model for the motion of the Philippine Sea Plate consistent with NUVEL-1 and Geological data. J. Geophys. Res. 98, 17,941-17,948.

Sowers, J.M., J.R. Unruh, W.R. Lettis, and T.D. Rubin (1994). Relationship of the Kickapoo fault to the Johnson Valley and Homestead Valley faults, San Bernardino County, California, *Bull. Seism. Soc. Am.*, 84, 528-536.

Thio, H.K. (1995). Source complexity of large strike-slip earthquakes. PhD Thesis, Caltech.

Wesnousky, S.G. (2008). Displacement and geometrical characteristics of earthquake surface ruptures: issues and implications for seismic-hazard analysis and the process of earthquake rupture, *Bull. Seism. Soc. Am.*, 98(4), 1609-1632, doi:10.1785/0120070111.

Wesnousky, S.G. (2006). Predicting the endpoints of earthquake ruptures. Nature 444, 358-360, doi:10.1038.

Xu Xiwei Xu,1 Guihua Yu,1 Y. Klinger,2 Paul Tapponnier,2 and Jerome Van Der Woerd (2006). Reevaluation of surface rupture parameters and faulting segmentation of the 2001 Kunlunshan earthquake (Mw7.8), northern Tibetan Plateau, China. J. Geophysical Research, 11, B05316, doi:10.1029/2004JB003488.

APPENDIX 1. FAULT RUPTURE MAPS OF LARGE STRIKE-SLIP EARTHQUAKES

Source: Wesnousky (2006)

No.	Date	Location	Type	Length (km)	M_w	Ref
1	1857-Jan-9	San Andreas, CA	ssr	360	7.9	1
2	1891-Oct-28	Neo-Dani, JPN	ssl	80	7.3	2
3	1930-Nov-2	Kita-Izu, JPN	ssl	35	6.7	3
4	1939-Dec-25	Erzincan, TUR	ssr	300	7.7	4
5	1940-May-19	Imperial, CA	ssr	60	6.9	5
6	1942-Dec-20	Erbaa-Niksar, TUR	ssr	28	6.8	4
7	1943-Nov-26	Tosya, TUR	ssr	275	7.5	4
8	1943-Sep-10	Tottori, JPN	ssl	10.5	6.2	6
9	1944-Feb-01	Gerede-Bolu, TUR	ssr	135	7.3	4
10	1967-Jul-22	Mudurnu, TUR	ssr	60	6.9	4
11	1968-Apr-8	Borrego Mtn, CA	ssr	31	6.1	7
12	1979-Oct-15	Imperial, CA	ssr	36	6.2-6.4	8,9
13	1981-Jul-29	Sirch Iran	ss	64	6.2	*10*
14	1987-Nov-23	Superstition Hills, CA.	ssr	25	6.2-6.4	11
15	1990-Jul-16	Luzon, PHL	ssl	112	6.9	12,13
16	1992-Jun-28	Landers, CA	ssr	77	7.2	14
17	1998-Mar-14	Fandoqa, IRN	ssn	25	6.6	10
18	1999-Oct-16	Hector Mine, CA.	ssr	44	6.9	15
19	1999-Aug-17	Izmit, TUR	ssr	145	7.1	16
20	1999-Nov-12	Duzce, TUR	ssr	40	7.0	17
21	2001-Nov-14	Kunlun, China	ssl	421	7.8	18-20
22	2002-Nov-03	Denali, AK	ssr	302	7.6	21

References

1. Sieh, K. E. Slip along the San Andreas Fault associated with the great 1857 earthquake. Bulletin of the Seismological Society of America 68, 1421-1448 (1978).
2. Matsuda, T. Surface faults associated with Nobi (Mino-Owari) Earthquake of 1891, Japan. Bulletin of Earthquake Research Institute, University of Tokyo 13, 127-162 (1974).
3. Matsuda, T. in Izu Peninsula (eds. Hoshino, M. & Aoki, H.) 73-102. (Tokai University Press, Tokyo, 1972).
4. Barka, A. Slip distribution along the North Anatolian Fault associated with the large earthquakes of the period 1939 to 1967. Bulletin of Seismological Society of America 86, 1238-1254 (1996).
5. Trifunac, M. D. & Brune, J. Complexity of energy release during the Imperial Valley, California, earthquake of 1940. Bulletin of Seismological Society of America 60, 137-160 (1970).
6. Kaneda, H. & Okada, A. Surface rupture associated with the 1943 Tottori earthquake: compilation of previous reports and its tectonic geomorphological implications. Active Fault Research 21, 73-91 (in Japanese with English Abstract) (2002).

7. Clark, M. M. (ed.) Surface rupture along the Coyote Creek fault, the Borrego Mountain Earthquake of April 9, 1968 (United States Geological Survey, 1972).

8. Johnson, C. E. & Hutton, L. K. Aftershocks and Preearthquake Seismicity in The Imperial Valley California, Earthquake of October 15, 1979. United States Geological Survey Professional Paper 1254, 59-76 (1982).

9. Sharp, R. et al. Surface faulting in the Central Imperial Valley in 'The Imperial Valley California, Earthquake of October 15, 1979. United States Geological Survey Professional Paper 1254 (1982).

10. Berberian, M. et al. The 1998 March 14 Fandoqa earthquake (Mw 6.6) in Kerman province, southeast Iran: re-rupture of the 1981 Sirch earthquake fault, triggering of slip on adjacent thrusts and the active tectonics of the Gowk fault zone. Geophy. J. Int. 146, 371-398 (2001).

11. Sharp, R. et al. Surface faulting along the Superstition Hills fault zone and nearby faults associated with the earthquakes of 24 November 1987. Bulletin of Seismological Society of America 79, 252-281 (1989).

12. Nakata, T. Surface faulting associated with the Philippine earthquake of 1990 (in Japanese). Journal of Geography 99, 95-112 (1990).

13. Yomogida, K. & Nakata, T. Large slip velocity of the surface ruptures associated with the 1990 Luzon earthquake. Geophysical Research Letters 21, 1799-1802 (1994).

14. Sieh, K. et al. Near-field investigations of the Landers earthquake sequence, April to July 1992. Science 260, 171-176 (1993).

15. Treiman, J., Kendrick, K. J., Bryant, W. A., Rockwell, T. K. & McGill, S. F. Primary surface rupture associated with the Mw 7.1 16 October 1999 Hector Mine earthquake, San Bernardino County, California. Bulletin of the Seismological Society of America 92, 1171-1191 (2002).

16. Barka, A. et al. The surface rupture and slip distribution of the 17 August 1999 Izmit Earthquake (M 7.4), North Anatolian Fault. Bulletin of Seismological Society of America 92, 43-60 (2002).

17. Akyuz, H. S. et al. Surface rupture and slip distribution of the 12 November 1999 Duzce Earthquake (M 7.1), North Anatolian Fault, Bolu, Turkey. Bulletin of Seismological Society of America 92, 61-66 (2002).

18. Klinger, Y. et al. High-resolution satellite imagery mapping of the surface rupture and slip distribution of the Mw ~7.8, 114 November 2001 Kokoxili earthquake, Kunlun fault, northern Tibet, China. Bulletin of the Seismological Society of America 95, 1970-1987 (2005).

19. Lin, A. et al. Co-seismic strike-slip and rupture length produced by the 2001 Ms 8.1 central Kunlun earthquake. Science 296, 2015-2017 (2002).

20. Xu, X., Chen, W., Ma, W., Yu, G. & Chen, G. Surface rupture of the Kunlunshan earthquake (Ms 8.1), northern Tibetan plateau, China. Seismological Research Letters 73, 884-892 (2002).

21. Haeussler, P. J. et al. Surface rupture and slip distribution of the Denali and Totschunda faults in the 3 November 2002 M7.9 earthquake, Alaska. Bulletin of the Seismological Society of America 94, S23-252 (2005).